

RESEARCH ARTICLE

10.1002/2016JB013874

Special Section:

Rock Physics of the Upper Crust

Key Points:

- Shale fracture initiation was revealed via correlative 4-D synchrotron X-ray tomography, digital volume correlation, and electron microscopy
- Fracture during accelerated shale maturation nucleates preferentially in laminated organic matter with initiation driven by mode I
- The coefficient of thermal expansion was quantified and found to be anisotropic relative to the bedding plane

Correspondence to:

P. D. Lee,
peter.lee@manchester.ac.uk

Citation:

Figueroa Pilz, F., P. J. Dowey, A.-L. Fauchille, L. Courtois, B. Bay, L. Ma, K. G. Taylor, J. Mecklenburgh, and P. D. Lee (2017), Synchrotron tomographic quantification of strain and fracture during simulated thermal maturation of an organic-rich shale, UK Kimmeridge Clay, *J. Geophys. Res. Solid Earth*, 122, 2553–2564, doi:10.1002/2016JB013874.



Received 22 DEC 2016

Accepted 20 MAR 2017

Accepted article online 23 MAR 2017

Published online 20 APR 2017

Synchrotron tomographic quantification of strain and fracture during simulated thermal maturation of an organic-rich shale, UK Kimmeridge Clay

Fernando Figueroa Pilz^{1,2}, Patrick J. Dowey³ , Anne-Laure Fauchille^{1,2}, Loic Courtois^{1,2}, Brian Bay⁴, Lin Ma^{1,2}, Kevin G. Taylor³, Julian Mecklenburgh³, and Peter D. Lee^{1,2} 

¹Manchester X-Ray Imaging Facility, School of Materials, University of Manchester, Manchester, UK, ²Research Complex at Harwell, RAL, Didcot, UK, ³School of Earth, Atmospheric, and Environmental Sciences, University of Manchester, Manchester, UK, ⁴Department of Mechanical Engineering, Oregon State University, Corvallis, Oregon, USA

Abstract Analyzing the development of fracture networks in shale is important to understand both hydrocarbon migration pathways within and from source rocks and the effectiveness of hydraulic stimulation upon shale reservoirs. Here we use time-resolved synchrotron X-ray tomography to quantify in four dimensions (3-D plus time) the development of fractures during the accelerated maturation of an organic-rich mudstone (the UK Kimmeridge Clay), with the aim of determining the nature and timing of crack initiation. Electron microscopy (EM, both scanning backscattered and energy dispersive) was used to correlatively characterize the microstructure of the sample preheating and postheating. The tomographic data were analyzed by using digital volume correlation (DVC) to measure the three-dimensional displacements between subsequent time/heating steps allowing the strain fields surrounding each crack to be calculated, enabling crack opening modes to be determined. Quantification of the strain eigenvectors just before crack propagation suggests that the main mode driving crack initiation is the opening displacement perpendicular to the bedding, mode I. Further, detailed investigation of the DVC measured strain evolution revealed the complex interaction of the laminar clay matrix and the maximum principal strain on incipient crack nucleation. Full field DVC also allowed accurate calculation of the coefficients of thermal expansion ($8 \times 10^{-5}/^{\circ}\text{C}$ perpendicular and $6.2 \times 10^{-5}/^{\circ}\text{C}$ parallel to the bedding plane). These results demonstrate how correlative imaging (using synchrotron tomography, DVC, and EM) can be used to elucidate the influence of shale microstructure on its anisotropic mechanical behavior.

Plain Language Summary Understanding the fracture of shale mudstones is important for determining how hydrocarbons form and move within shales, and it also helps us understand the environmental impact of extracting those hydrocarbons. Although we cannot see into shales, using the powerful X-rays from a synchrotron, we can take tomograms (a 3-D image like computer-aided tomography scans) of a shale every second or so, giving us a 4-D image (3-D plus time). 4-D imaging not only reveals the fractures but also allows us to quantify how the texture of the minerals and organics in the shales moves with time (called digital volume correlation or DVC). This DVC technique lets us calculate the strains around the fractures before they form and as they grow. These strain fields help us understand where fractures will form, how they grow, and characterize the crack opening mode (or state of applied stress and strain) causing them to form. The correlative imaging technique developed was used to watch fractures form in a shale during accelerated maturation (aging over time and temperature). This demonstration shows how correlative imaging (using synchrotron tomography, DVC, and electron microscopy) can be used to elucidate the influence of shale microstructure on its fracturing properties.

1. Introduction

Production from unconventional shale reservoirs has increased significantly over the last decade as a result of improved technology and increased economic viability [Durham, 2008; Biewick, 2013]. Understanding the timing, initiation, and development of natural fracture networks within shale reservoirs is critical. These networks provide pathways for fluids to reach the wellbore contributing directly to the location of potential sweet spots [Pervukhina et al., 2015]. Quantifying the mechanisms of natural fracture generation could provide an insight into development of hydraulically induced fractures during production, as they control the extraction of hydrocarbons from organic-rich mudstones [Druyff, 1991; Duhaillan and Sonnenberg, 2014]. Fracture studies on

recovered core material from shale reservoirs are problematic, as organic matter (OM) within the sample has undergone at least partial maturation and the rock experiences depressurization that could result in artificial fracture development. However, studying the development and mechanisms of fracture development under experimental maturation of immature organic-rich shale from outcrop sources can minimize these issues.

During maturation, temperature-dependent mechanisms take place, driven by the transformation of kerogen into hydrocarbons, especially gas, that result in the formation of cracks [e.g., *Michels et al.*, 1994]. Horizontal cracks propagate at subcritical stresses due to the strong microstructural fabric and the associated anisotropy in mechanical properties. This anisotropy is due to both the layered deposition and geometrical characteristics of the kerogen laminar inclusions [e.g., *Ozkaya*, 1988; *Engelder and Lash*, 2008]. Further, the path by which cracks propagate is directly linked to the in situ stress and strain field, as suggested by *Lash and Engelder* [2005]. Two-dimensional analytic models have been proposed to estimate the stress and strain required to propagate collinear crack opening under a single mode of fracturing [*Wackertapp et al.*, 2000; *Olson*, 2004; *Jin et al.*, 2010]. However, there is a paucity of data to validate these models. A few prior studies have qualitatively described the microstructure and crack dynamics by using ex situ scanning electron microscopy (SEM) observations [*Uvarova et al.*, 2014], mineralogy investigations [*Pervukhina et al.*, 2015], and synchrotron X-ray tomography (sCT) data [*Yurikov et al.*, 2013; *Patrusheva et al.*, 2014], but in situ quantitative data are lacking.

In situ radiography [*Lee and Hunt*, 1997] and synchrotron X-ray tomography (sCT) have become key tools and are now regularly used to quantify crack and other defect formation in a wide range of fields. These include metallic alloy micromechanics to granular flow and even the cracking of high-temperature semisolid metals [*Kareh et al.*, 2014; *Karagadde et al.*, 2015]. They have also been used in a number of geological applications, such as observing the influence of fabric in soils to shear band formation [*Fonseca et al.*, 2013].

The use of time-resolved synchrotron X-ray tomography on samples ranging from 1 to hundreds of millimeters and resolutions as good as near 1 μm offers the unique advantage of being able to quantify structures and even strain development during fracturing. The evolution of the strain field during deformation can be quantified via analyzing 4-D sCT images by using digital volume correlation (DVC), a three-dimensional extension of digital image correlation [*Bay*, 2008]. Using DVC it is possible to correlate fluctuations in displacement with changes in microstructure during sample deformation. This method avoids the use of complex X-ray diffraction approaches [*R  thor   et al.*, 2011].

In the context of shales, *Kobchenko et al.* [2011] and *Panahi et al.* [2012] used synchrotron tomography to characterize and describe the dynamics and patterns of cracks at microscale. Their work demonstrated the potential power of sCT in such field and how the data can be used to model the fracture behavior during heating overpressuring [*Teixeira et al.*, 2017]; however, no 3-D strain mapping was performed.

In this study, synchrotron tomography coupled with digital volume correlation was used to quantitatively investigate fracture phenomena during a simulated maturation of a Kimmeridge Clay sample. For the first time, the magnitude and the direction of the principal strains around fractures were quantified in 3-D to elucidate the opening modes as the maturation progressed. These results are used to advance our understanding of crack initiation and propagation mechanisms. A brief description of the experimental setup, followed by an in-depth description of the DVC technique, is presented first. The sCT results are then correlated to SEM and transmitted light microscopy data to provide new insights into the relative roles of organic and inorganic phases upon fracture nucleation.

2. Material and Methods

2.1. Material

2.1.1. Kimmeridge Clay

An outcrop sample of Kimmeridge Clay, from the Blackstone Band, east of Kimmeridge Bay (Dorset), UK, was selected for this study due to the following: (i) its high organic content and primary mud-rich lithology; (ii) its relative thermal immaturity (burial to a lower temperature than the oil window); and (iii) it is one of the most prolific source rocks in Europe, sourcing much of the North Sea reserves [*Faber and Stahl*, 1984; *Fishman et al.*, 2012].

Kimmeridge Clay is an Upper Jurassic organic-rich mudstone deposited in a series of basins from eastern Greenland, Canada to Norway, and south of England [*Dore et al.*, 1985]. Kimmeridge Clay exhibits a wide

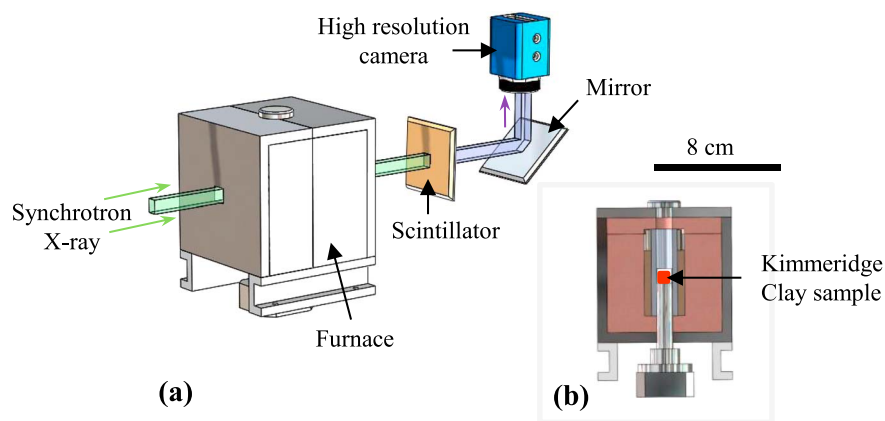


Figure 1. (a) Schematic of sCT experimental setup. (b) Cross section of the high-temperature furnace showing the sample in rotation stage for tomography.

range of total organic carbon (TOC), from below 2 wt % to 60 wt % in some cases [van Kaam-Peters *et al.*, 1998; Tyson, 2004]. Continuous and elongated organic particles are present in low TOC intervals, whereas the organic matter is structured in thick laminations in high TOC samples [Boussafir *et al.*, 1995]. The microstructure of Kimmeridge clay rocks varies with the location and the facies, but it is usually seen as an alternation of mudstones, limestones, bituminous and oil shale, and sandy facies [Oschmann, 1988]. Amorphous organic matter is dominant [Tyson, 1989], but sharp flakes, heterogeneous flocks, and opaque aggregates can also be present [Boussafir *et al.*, 1995]. The abundance of OM is variable and shows microcycles, mainly due to a balance between the nature of deposited biomass and variable deposition conditions [Ramanampisoa and Disnar, 1994; Boussafir *et al.*, 1995; Desprairies *et al.*, 1995].

The sample chosen in this study is from the shaly oil facies and has a size of $3 \times 3 \times 7 \text{ mm}^3$. For outcrop lithofacies, the Kimmeridge Clay is usually composed of 20–65% of clay minerals (mainly illite, kaolinite, and lower contents of smectite and chlorite), quartz or fine-grained sand (12–40%), carbonates (15–40%), pyrites, and kerogen [Morgans-Bell *et al.*, 2001; van Dongen *et al.*, 2006].

2.1.2. Sample Preparation

Before the sCT experiment, a subset of the sample was prepared as a thin section and analyzed by using transmitted light and scanning electron microscopy (SEM) with standard polishing products. After the simulated maturation and in situ sCT experiment, the surface effects of maturation on the heated sample were first optically imaged, then the sample was mounted in epoxy resin on a glass slide, and approximately third of the sample volume was removed ($1 \times 1 \times 6 \text{ mm}^3$) through polishing, using standard mechanical thin-section polishing techniques. A large mosaic of high-resolution backscattered electron SEM images was then acquired at 20 kV with a magnification of 2000 and a resolution of $0.16 \mu\text{m pixel}^{-1}$ to investigate the microstructure after heating. The mineral phases (tectosilicates, carbonates, organic matter, and clay matrix) are visible under SEM, but only groups of minerals are visible with phase contrast in sCT scans due to lower resolution ($0.81 \mu\text{m voxel}^{-1}$).

2.2. Methods

2.2.1. Synchrotron Maturation Experimental Setup

The unconfined maturation experiment was performed at the Diamond Manchester Branchline, Diamond Light Source (Figure 1a). A high-temperature furnace designed for in situ tomography [Puncreobutr *et al.*, 2012, 2013] was used. The sample was held in a rotating ceramic holder with ceramic wool as packing and placed inside the furnace (Figure 1b). Once in position, the temperature was increased from 20°C to 400°C at a rate of $2^\circ\text{C}/\text{min}$ without interruption. The temperature was monitored by a thermocouple mounted at the inner top corner of the furnace.

The distance between the scintillator and the furnace was set to 60 mm. A high-resolution camera (PCO Edge) was used with 4X magnification. An effective pixel size of $0.81 \mu\text{m}$ in a field of view of $2.1 \times 1.8 \text{ mm}^2$ was achieved. The tomography data sets consisted of 1800 projections taken using monochromatic X-rays (20 keV) over a 180° rotation angle. Acquisition time was 2 min, and tomograms were taken every 50°C until

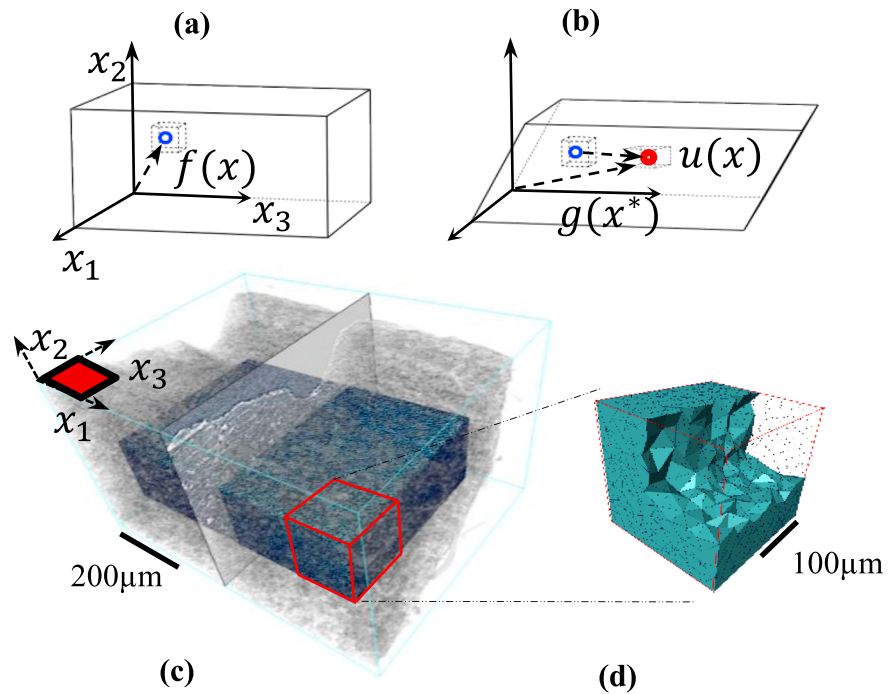


Figure 2. Schematic of the DVC method. (a) Reference volumetric image with a single subvolume and (b) deformed volumetric image. The labels x and x^* refer to the coordinates of the subvolumes in the reference and deformed configurations. The label $u(x)$ is used to describe the displacement field, and f and g are the grey scale values of the reference and deformed states, respectively. (c) 3-D rendering of Kimmeridge Clay sample with the selected region of interest (ROI). (d) A subsection of the point cloud used to track local subvolumes.

200°C, and then every 10°C above this temperature. Radiography was used to observe sample behavior between tomographs.

A filtered back projection algorithm [Titarenko et al., 2010; Kyrieleis et al., 2011] was used to reconstruct the 3-D tomographic data sets. Each reconstructed data set consisted of an 8-bit grey scale volume of $1000 \times 770 \times 1215 \mu\text{m}^3$. The rigid body motion was eliminated using a 3-D registration method [Schneider and Eberly, 2002] in Avizo 8.1 (FEI, USA).

2.2.2. Digital Volume Correlation

Digital volume correlation (DVC) is a technique for noncontact displacement and strain measurement and can be considered a three-dimensional extension of digital image correlation [Bay, 2008]. The DVC process for calculating displacement fields involves three main steps: (i) the discretization of the tomographic data into many subvolumes, each tracked by using a central point (forming a point cloud) (Figures 2a and 2d); (ii) the determination of the motion of each individual point and its local subvolume by using the cross correlation of the volumetric images (Figures 2a and 2b); and (iii) the estimation of relative displacement and strain fields for each volumetric elements [Bay et al., 1999]. In this work, we selected a region of interest of $770 \times 690 \times 365 \mu\text{m}^3$ and a mesh with 115,000 randomly distributed nodes in the point cloud. The average distance between the nodes of the mesh was $13 \mu\text{m}$ (Figures 2c and 2d). Each point was considered the center of a cubic subvolume with an edge length of $26 \mu\text{m}$; hence, each subvolume was approximately 50% overlapped.

The relative displacements were calculated with an in-house DVC code and used to evaluate the Green-Lagrange finite strain tensor (F) [Bay et al., 1999]. The deformation tensor contains the principal strains (e_1 , e_2 , and e_3) which are independent of the orientation of the coordinate system. The directions (eigenvectors) in which these strains act were also determined. Finally, the volume change (ϵ_v) was calculated from the volumetric strain by using the Jacobian of the transformation tensor from Green-Lagrange formulation [Bazant, 1996]:

$$\epsilon_v = \det(F) = (1 + e_1)(1 + e_2)(1 + e_3) \quad (1)$$

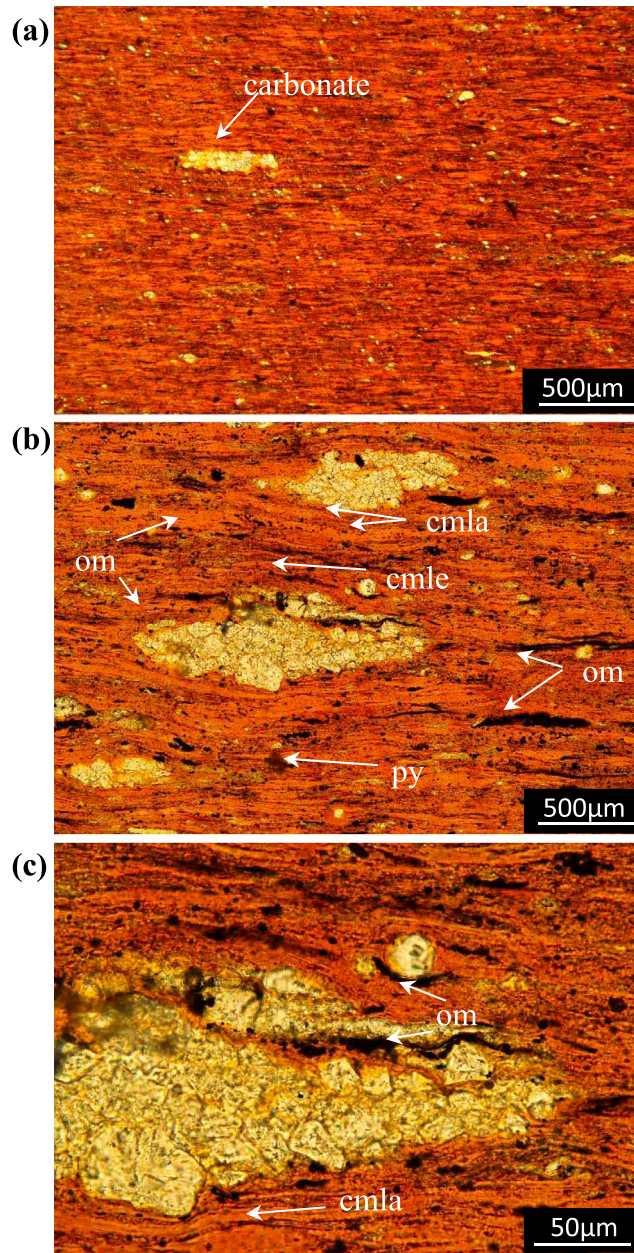


Figure 3. Microstructure and fabric of the Kimmeridge Clay sample before maturation: (a) low-magnification plane-polarized light (PPL) image showing a laminar fabric orientated in the bedding direction (horizontal) and (b and c) medium magnification PPL images showing pyrite (py) and organic matter (OM): orange-red and black elongate lamina grains, orientated parallel to bedding. Clay minerals are also present: clay mineral lamina (cmla) and clay mineral lens (cmle).

3. Results and Discussion

3.1. Microstructural Characterization

Petrology of the unheated sample is shown in Figure 3. The total organic carbon (TOC) content of the sample analyzed was 36 wt %, which is similar to a previous study on The Blackstone Band of the Kimmeridge Clay

As part of the DVC process, the objective function was calculated with a normalized sum of square differences, $C(x)$:

$$C(x) = \frac{\iint [Q(x^*) - P(X)]^2}{\sqrt{\iint [Q(x^*) - P(X)]^2}} \quad (2)$$

This function is represented by a non-negative value that quantifies the degree of match of a given sub-volume (s) between the reference, $f(x)$, and deformed state, $g(x^*)$ [Bay, 2008]; it tends to converge toward 0 when the difference between f and g is small. The uncertainty was then calculated by computing the relative changes between tomographic data sets taken at the same temperature and by determining the standard deviations of the histograms of displacement.

The increase in the objective function $C(x)$ is reflected by a widening of the histogram and an increment in the standard deviation of its distribution. The maximum objective function value at 370°C was calculated as 0.01 [Réthoré et al., 2011]. The calculated displacements and strains were converted into color-scaled volumetric images and superimposed onto grey scale tomographic data. The measurements at local discontinuities are less accurate; therefore, values along the border of cracks should be taken as estimates [Poissant and Barthelat, 2009].

The concentration of carbonates and clays was also color mapped as estimated from the X-ray attenuation values in the volumetric image [Wallisch et al., 2014], allowing correlation of the distribution of minerals and clays to the DVC-calculated displacements and strains as a function of temperature.

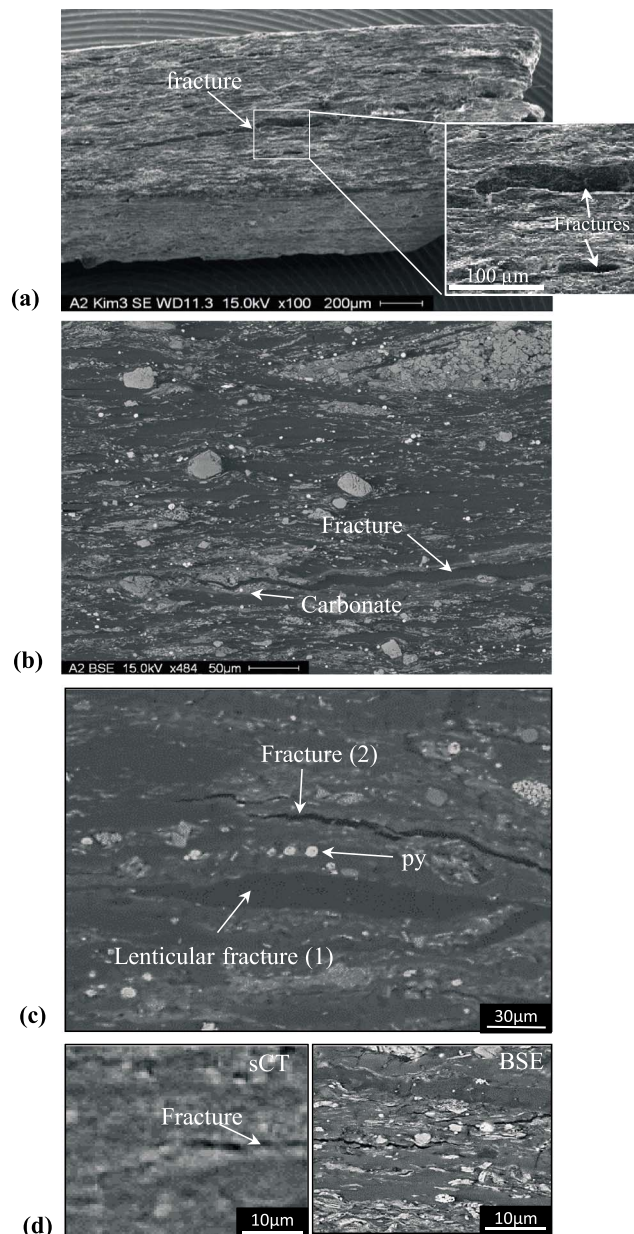


Figure 4. (a) SEM-SE observation of sample surface roughness after maturation, (b) SEM-BSE micrographs of large fracture on the surface of the sample after maturation, (c) lenticular fracture on sample surface under SEM-BSE, and (d) side-by-side comparison between sCT and SEM-BSE image of a fracture.

cracks ~20–100 µm long and 5–30 µm high (note, most are filled with resin) and (2) thin, narrow cracks (less than 5 µm) (Figures 4c and 4d). In many cases the cracks were directly correlated between the CT and SEM images (Figure 4d). This allowed observation of the opening and closing of lenticular fractures from the CT time series: a phenomenon hypothesized to result from organic matter gas formation and release during heating. The cracks (2) are thin and tortuous and appear to be unfilled by the resin, suggesting that they are not well connected to the sample boundaries or large lenticular fractures. Moreover, Figure 4d shows that these cracks (2) were present during maturation and did not result from sample preparation for SEM imaging.

Organic matter observed before the experiment underwent pyrolysis. This was confirmed with EDS by a decrease of sulfur and carbon and may indicate sulfur dioxide release during pyrolysis. Due to experimental

[van Dongen *et al.*, 2006]. Different phase groups were identified as organic matter, clay minerals, carbonates, and pyrite. The predominant amorphous phase is organic matter (OM) present as orange-red elongated laminated zones (Figures 3b and 3c) parallel to bedding (20–300 µm long, 5–20 µm thick). Organic matter boundaries are marked by subtle color differences between grains and the presence of other detrital or authigenic minerals. Clay minerals are interbedded with organic matter and oriented parallel to bedding. Clay minerals are present in two forms (Figures 3b and 3c): clay mineral lamina (cm_{la}) and clay mineral lens (cm_{le}). The carbonates are agglomerated in elongated clusters, and their origin was interpreted as carbonate-cemented foraminifera (Figures 3a–3c). The pyrites have a framboidal morphology within carbonate clusters and clay mineral and organic matrix (Figures 3b and 3c).

After heating, the microstructure was studied using scanning electron microscopy (SEM) with backscattered electron (BSE) at a resolution of 0.16 µm pixel⁻¹ (Figure 4). The phases were confirmed by using electron diffractive spectroscopy (EDS). Macroscopic (whole specimen) SEM analysis revealed a rough surface, with open fractures (~2000 µm long) from the top edge of the sample oriented along bedding (Figure 4a). Higher magnification images (Figures 4b and 4c) highlight two different types of horizontal fracture, both parallel to the bedding planes: (1) large, lenticular, ellipsoidal

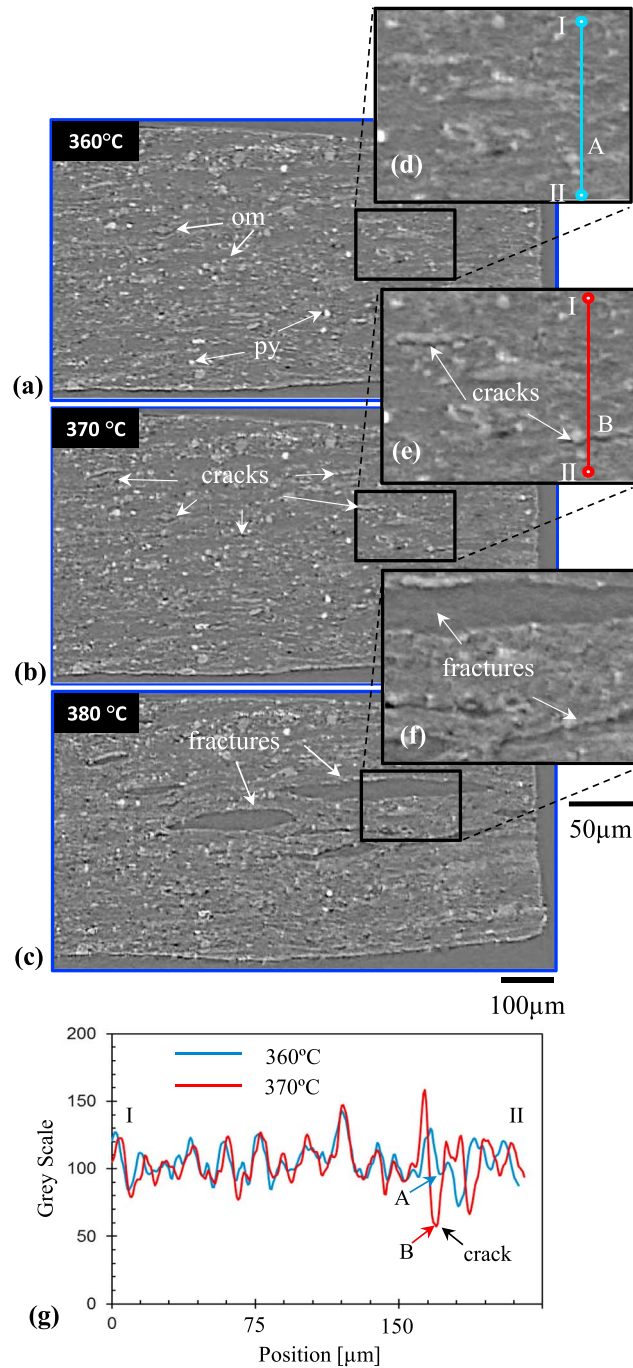


Figure 5. Single attenuation slices at different temperatures: grey scale tomographic slices at (a) 360°C, (b) 370°C, and (c) 380°C, respectively; (d–f) enlarged 220 × 190 μm box of Figures 5a–5c images, respectively; and (g) line plots of attenuation intensity at 360°C and 370°C corresponding to the portion crossed by the red line in Figures 5d and 5e. The locations A and B point to an area where the crack nucleates, and this behavior is reflected by a decrease in the attenuation values.

dilation of the sample between temperatures. Between 370°C and 380°C, the sample undergoes rapid deformation and a distinct set of new fracture surfaces forms (Figures 5d–5f).

The average displacements for temperatures from 200°C and 370°C are shown in Figure 6. Note that the displacements due to the very large fracture displacements at 380°C were too great for effective DVC displacement

factors (cooling from 380°C changed the structure of the sample), only an approximate manual matching of the SEM images to the sCT tomographic data was possible. Major features on the same plane could be matched (Figure 4d), but a full correlation was not possible. Comparison between SEM and sCT data shows that cracks generated during maturation are located in the organic matter and clay mineral matrix, or at the interface between these phases and the inorganic phase. Cracks were observed at the boundaries of mineralogical heterogeneities such as at the interface between large, coarse grains of carbonate and pyrite where local variations in mechanical properties cause stress concentrations (Figure 4d). The fractures are tortuous and discontinuous in the 2-D SEM images.

3.2. Strain Measurement: Crack Initiation and Propagation

A set of sCT tomographic slices perpendicular to the bedding at temperatures from 360°C to 380°C are shown in Figures 5a–5c. Below 200°C, grey scale changes in the sCT volumetric images are subtle. Above 200°C, thermal expansion is visible, but only at 360°C is fracturing prevalent at the scale and resolution used in this study. Comparing 2-D slices from the tomographic volume data sets at 360°C and 370°C reveals small fractures open at 370°C (Figures 5a and 5b). Line plots of the attenuation intensity from these two temperatures are compared in Figure 5g, with regions of incipient fractures having lower attenuation intensities (marked with A and B). The offset of the peaks from the more attenuating mineral phases shows the

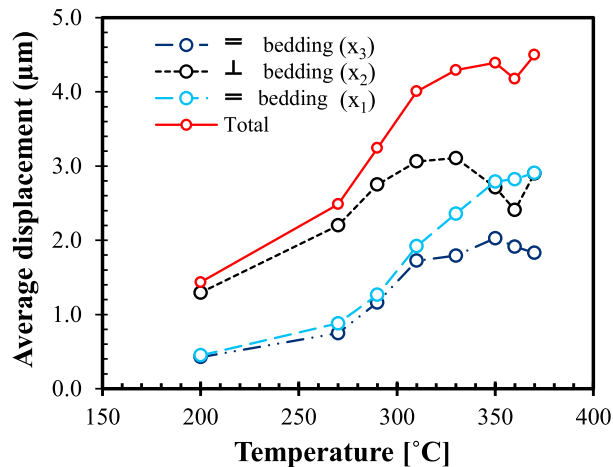


Figure 6. Progression of the calculated average DVC displacement (absolute value, integrating displacements due to both thermal expansion and cracking) in the three directions x_1 , x_2 , and x_3 , described by the subvolumes in the region of interest.

tracking; i.e., the maximum fracture opening ($\sim 70 \mu\text{m}$) exceeds the average edge length of the selected subvolume ($26 \mu\text{m}$). Above 200°C , gases are evolving, driving volumetric expansion. Expansion is preferentially accommodated perpendicular to bedding due to the horizontal layering of organic matter and clay minerals. The volume expands until $\sim 320^\circ\text{C}$, slowly at first. Above 250°C , the rate of expansion increases—at this temperature, fractures were seen to form and grow (as observed in the real-time radiography). Above 320°C , these fractures collapsed occasionally, presumably as gas is released to the exterior surface, frequently reforming. This is thought

to cause the fluctuations in expansion. We hypothesize that these cracks form due to increasing pressure from kerogen decomposition, with differential expansion providing nucleation sites at the interfaces between phases. The fluid pressure in the pore space of kerogen may also influence crack formation [Zargari *et al.*, 2016], but was difficult to investigate in our study.

Quantifying the regions of high strain can be used as an indicator to predict crack locations. During the crack expansion, the strain maps can also be used to track the local deformation around the cracks. Figure 7a is a plot of the volumetric strain in a selected region of interest and the average maximum principal strain (ϵ_1). For each temperature, the strain pattern is given in Figures 7b–7e.

Figures 7b–7e show small subvolumes ($100 \times 100 \times 90 \mu\text{m}$) of an observed fracture at high temperatures. The figure displays values of integrated strain greater than 0.01 as a cloud plot with increasing temperature. These strain maps show the highly localized nature of the strain. The coefficient of thermal expansion is directly calculated from the average strain. It has the value of $8 \times 10^{-5}/^\circ\text{C}$ perpendicular to bedding and $6.2 \times 10^{-5}/^\circ\text{C}$ parallel to the bedding plane over the temperature range of 100 – 350°C (until fracture expansion and collapse occurred). Comparison of the strain contours with the attenuation image shows that strain is concentrated in the clay mineral phase (light grey). Due to the shale fabric, the strain is elongated in the plane of the bedding. As the temperature increases (Figures 7b–7e), we track the growth of the region of high strain. The evolution of strain within the different mineral/organic phases is thus mapped before the fracture forms, allowing temperature-dependent mechanisms leading to fracture initiation to be observed.

During the heating phase between Figures 7b and 7c (200 – 330°C) the volume of high strain has grown significantly as internal gas pressure builds. At 350°C (Figure 7d) the strain in this volume is reduced, which matches the reduction in total strain (Figures 6 and 7a). This reduction in the principal strain is interpreted to be caused by the initial release of gas to the exterior of the sample, based on radiograph observation of the opening and closing of fractures at temperatures above 360°C . This interpretation is further supported by the thermogravimetry measurements by Kobchenko *et al.* [2011] in a Green River Shale, where organic matter transformation into volatile hydrocarbons initially occurred in a temperature range of 350 – 370°C .

The increment in strain between 350°C and 370°C , due to partial release of gas pressure, matches well with the measurements by other authors of a slight increase in fracture toughness with temperature, owing to increased inter-granular friction as the clay matrix dehydrates [Ibanez and Kronenberg, 1993]. At 370°C , cracks appear in the attenuation image (Figures 7e and 5b) and the maximum principal strain calculated from DVC increases significantly (Figure 7a). Peak strains were localized around the crack opening, and the direction of the eigenvectors driving the opening mode is predominantly perpendicular to the bedding plane (Figure 7f).

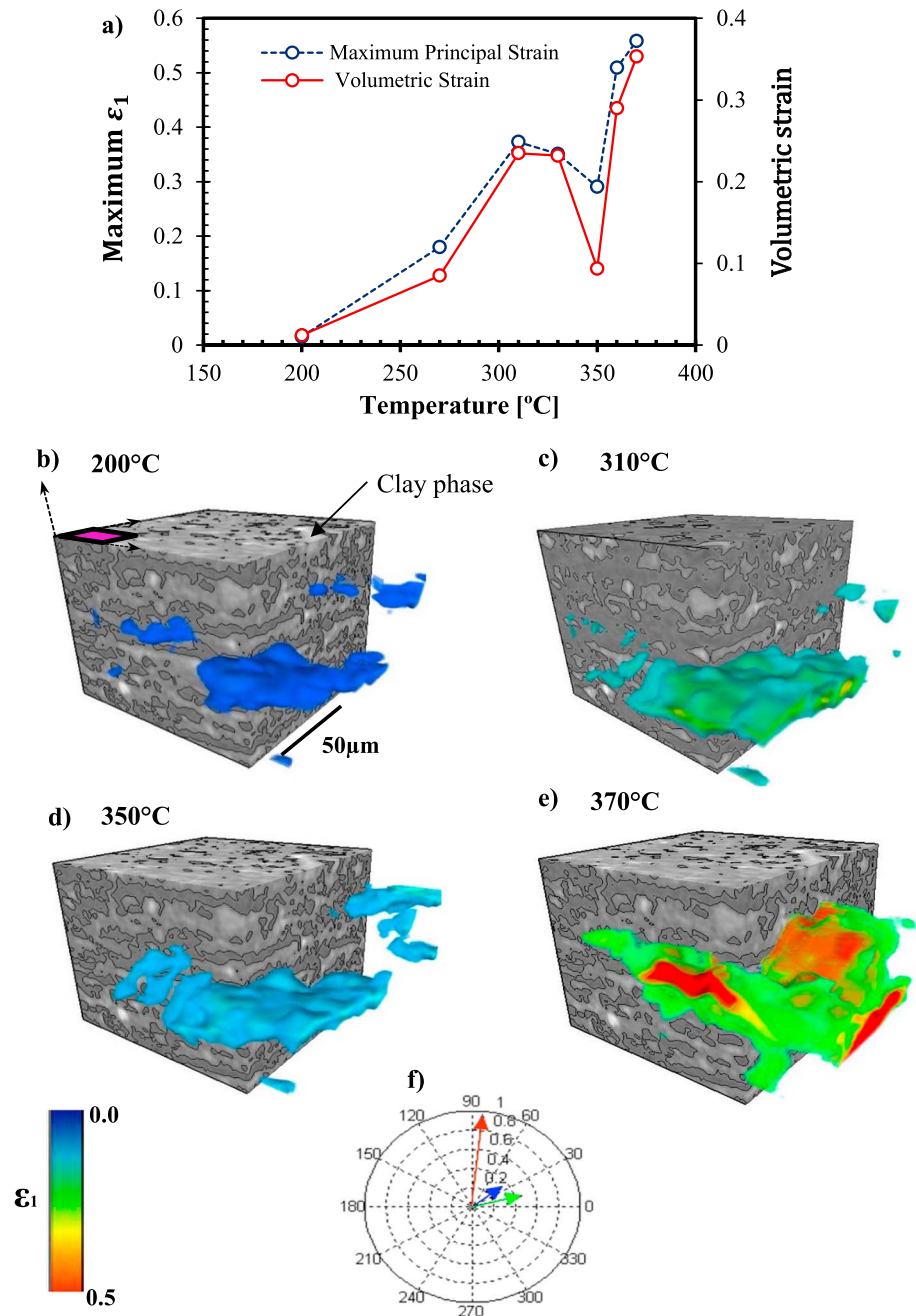


Figure 7. Progression of the average maximum principal strain in a small subvolume. The volumetric strain of the region of interest is presented to show the change in values throughout the maturation. (a) Maximum principal strain and volumetric strain. Cloud plot of the ϵ_1 in a selected subvolume of $100 \times 100 \times 90 \mu\text{m}$ with a cut-out of 0.05 at (b) 200°C, (c) 310°C, (d) 350°C, and (e) 370°C. The markers represent some of the scanning temperatures when sCT data were acquired. (f) Eigenvector components at 370°C.

Therefore, we suggest that the main mode driving fracture nucleation is opening displacements perpendicular to the bedding (mode I), although the shear parallel to the crack and the out-of-phase displacement perpendicular to the bedding (modes II and III) are also involved. Previous models have considered mode I as the main fracture opening driver to establish analytical relationships for subcritical propagation [Wackertapp et al., 2000; Holder et al., 2001; Jin et al., 2010], and here we present a combination of tools to effectively validate this hypothesis in situ.

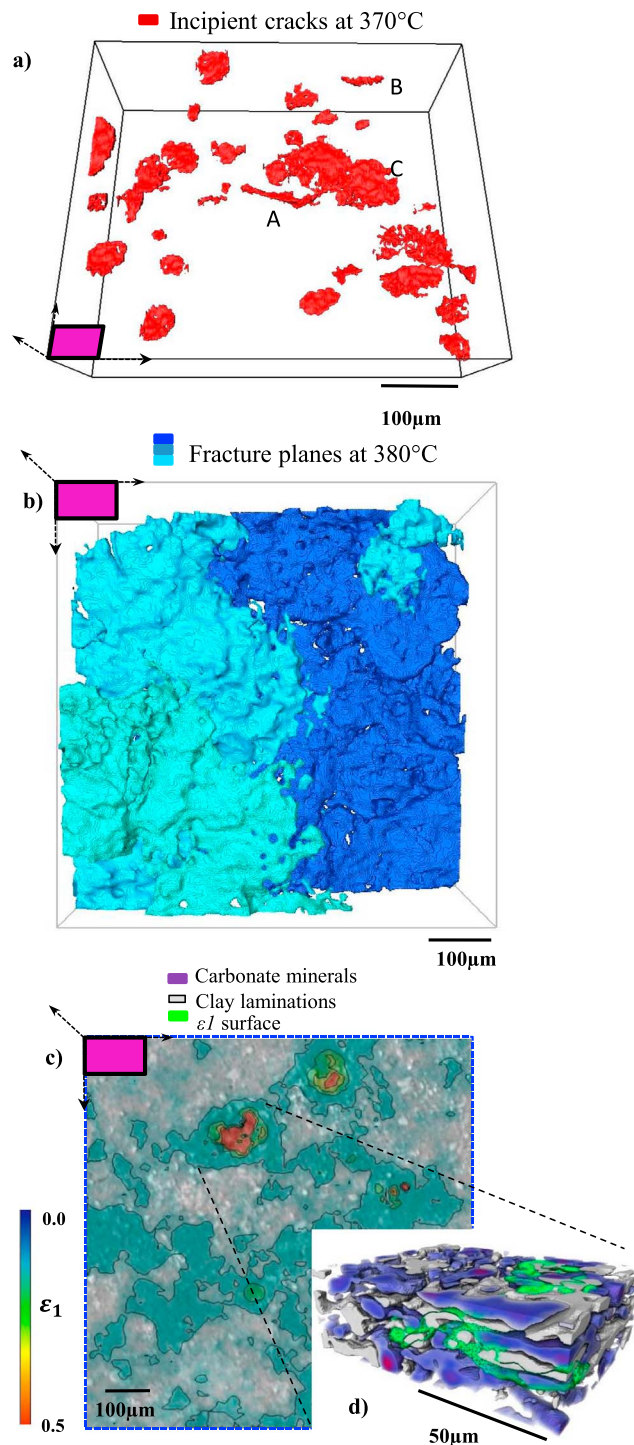


Figure 8. (a) Cracks imaged in a sample heated at 370°C by using DVC strain to aid segmentation. Some of the cracks grow at mineral interfaces (A and B), but most of the cracks are penny shaped (C) and grow in the laminar organic matter. (b) Fracture plane imaging at 380°C. (c) Superimposed maximum principal strain ϵ_1 at 370°C with attenuation values in a slice parallel to bedding plane. (d) 3-D distribution of carbonates-clays and maximum principal strain.

The DVC measurement of principal strain also aided in the segmentation process for isolating and quantifying the final fractures (Figure 8). Significant difficulties in shale segmentation due to the low variation in attenuation contrast have been previously reported [Kanitpanyacharoen *et al.*, 2013]. By correlating the regions of high-integrated principal strain at 370°C from DVC maps to the attenuation data and mineral distribution maps, the regions of both developed fractures and also those of incipient cracks (defined as having a maximum opening thickness of 5 µm) could be identified via thresholding (Figure 8a). Segmented cracks at 370°C (Figure 8a) appear to nucleate preferentially in the laminated organic matter. This is probably due to increasing gas pressure between layered mineral clusters during maturation. Once nucleated, the cracks often grow as thin features around mineral interfaces. These segmented cracks at 370°C can be also compared in location with the fracture planes at 380°C (Figure 8b). This suggests that fracture propagation occurs through the coalescence of smaller cracks parallel to bedding (Figures 7e and 5c, 5e, and 5f). Comparison of Figures 8c and 8d highlights the difference in resolution between sCT and SEM-BSE. Figure 8c is an SEM-BSE image, which provides a higher resolution image but only in 2-D. If we superimpose the strain calculated by using DVC on the sCT images on this image, it allows us to further correlate the areas of strain and incipient cracking to the local microstructure and its fabric. Using correlative imaging, we can extract the region of highest strain and display it in 3-D from the sCT images as shown in Figure 8d. Surface rendering distinguishes carbonate minerals (purple), clay laminae (grey), and organic phases (invisible). A contour with strain values of 0.25 (green) occurs

within the organic and clay mineral phases and is present at the interface between these phases and inorganic carbonate minerals but is not found within the carbonates. Figures 4–8 demonstrate how correlative imaging using sCT, DVC, and SEM can be used to qualitatively and quantitatively characterize the deformation and fracture behavior of the organic-rich shale, Kimmeridge Clay.

4. Conclusions

In this study, a sample of Kimmeridge Clay (UK) was imaged by using time-resolved synchrotron X-ray tomography while being subjected to an accelerated maturation process between 20 and 380°C. Correlative imaging using scanning electron microscopy was performed before and after maturation. Three-dimensional strain mapping and fracture development were quantified by digital volume correlation during the maturation to quantify the sample's deformation and fracturing. In combination with SEM data, the application of DVC techniques to sCT data provides a powerful tool to unravel the complex anisotropic behavior in shales during unconfined simulated maturation. During heating the Kimmeridge Clay was shown to behave anisotropically, with distinct coefficients of thermal expansion measured parallel (8×10^{-5}) and perpendicular (6.2×10^{-5}) to bedding. Quantification of eigenvector directions before crack propagation suggests that the main mode driving the crack initiation is the opening displacement perpendicular to the bedding (mode I). The location of the incipient cracks indicates that they nucleate preferentially in the laminated organic matter between layered mineral clusters. These incipient cracks merge to form horizontal fractures, following the path of maximum principal strain through the clay mineral matrix. Fracture formation was quantified in three dimensions including the mapping of the surrounding strain field. The fractures and strain field were correlated to the mineral and organic phases. Further application of this combination of techniques will provide a powerful tool to extract real-time information about fracture behavior in shales during simulated loading scenarios.

Acknowledgments

F.P. gratefully acknowledges support from the University of Manchester and the Mexican Council of Science and Technology, CONACyT. This project was funded in part by the Diamond-Manchester Collaboration, the Research Complex at Harwell, the NERC (NE/M001458/1), and the EPSRC (EP/I02249X/1). A.L.F., P.D.L. and K.T. were supported in part by the European Union's Horizon 2020 716 Research and Innovation Programme under the ShaleXenvironment project (grant 640979). The synchrotron imaging was performed at the Diamond-Manchester Branchline of Diamond Light Source (DLS), Beamtime MT9866-1. Data statement: representative research data are presented in the images and graphs in this manuscript.

References

- Bay, B. K. (2008), Methods and applications of digital volume correlation, *J. Strain Anal. Eng. Des.*, *43*(8), 745–760.
- Bay, B. K., T. S. Smith, D. P. Fyhrrie, and M. Saad (1999), Digital volume correlation: Three-dimensional strain mapping using X-ray tomography, *Exp. Mech.*, *39*(3), 217–226.
- Bazant, Z. P. (1996), Finite strain generalization of small-strain constitutive relations for any finite strain tensor and additive volumetric deviatoric split, *Int. J. Solids Struct.*, *33*(20), 2887–2897.
- Biewick, L. R. H. (2013), Map of assessed shale gas in the United States, 2012, U.S. Geol. Surv. Digital Data Ser. 69–Z, 16.
- Boussafir, M., F. Gelin, E. Lallier-Verges, S. Derenne, P. Bertrand, and C. Largeau (1995), Electron microscopy and pyrolysis of kerogens from the Kimmeridge Clay Formation, UK: Source organisms, preservation processes, and origin of microcyles, *Geochim. Cosmochim. Acta*, *59*, 3731–3747.
- Desprairies, A., M. Bachaoui, A. Ramdani, and N. P. Tribouillard (1995), Clay diagenesis in organic-rich cycles from the Kimmeridge Clay Formation of Yorkshire (G.B.): Implication for palaeoclimatic interpretations, in *Lecture Notes in Earth Sciences*, vol. 57, pp. 63–91, Springer, Berlin.
- Dore, A. G., J. Vollset, and G. P. Hamar (1985), Correlation of the off shore sequences referred to the Kimmeridge Clay Formation: Relevance to the Norwegian Sector, in *Petroleum Geochemistry in Exploration on the Norwegian Shelf*, edited by B. M. Thomas, pp. 27–37, Graham & Trotham, London.
- Druyff, L. (1991), Reservoir properties of the Bakken Shale, in *Geology and Horizontal Drilling of the Bakken Formation, Guidebook*, edited by W. B. Hansen, 91 pp., Montana Geol. Soc.
- Duhailan, M., and S. Sonnenberg (2014), The curious case of hydrocarbon-expulsion fractures: Genesis and impact on the Bakken Shales, in *AAPG Annual Convention and Exhibition*, p. 30, Houston, Tex., 6–9 April.
- Durham, L. S. (2008), Prices, technology make shales hot, *AAPG Explorer*, 10.
- Engelder, T., and G. Lash (2008), Marcellus Shale Play's vast resource potential creating stir in Appalachia, *The American Oil & Gas Reporter* (May), 7.
- Faber, E., and W. Stahl (1984), Geochemical surface exploration for hydrocarbons in North Sea, *AAPG Bull.*, *68*, 363–386.
- Fishman, N. S., P. C. Hackley, H. A. Lowers, R. J. Hill, S. O. Egenhoff, D. D. Eberl, and A. E. Blum (2012), The nature of porosity in organic-rich mudstones of the Upper Jurassic Kimmeridge Clay Formation, North Sea, offshore United Kingdom, *Int. J. Coal Geol.*, *103*, 32–50.
- Fonseca, J., C. O'Sullivan, M. R. Coop, and P. D. Lee (2013), Quantifying the evolution of soil fabric during shearing using directional parameters, *Geotechnique*, *63*(6), 487–499.
- Holder, J., J. E. Olson, and Z. Philip (2001), Experimental determination of subcritical crack growth parameters in sedimentary rock, *Geophys. Res. Lett.*, *28*, 599–602, doi:10.1029/2000GL011918.
- Ibanez, W., and A. Kronenberg (1993), Experimental deformation of shale: Mechanical properties and microstructural indicators of mechanisms, *Int. J. Rock Mech. Mining Sci.*, *30*(7), 723–734.
- Jin, Z. H., S. E. Johnson, and Z. Q. Fan (2010), Subcritical propagation and coalescence of oil-filled cracks: Getting the oil out of low-permeability source rocks, *Geophys. Res. Lett.*, *37*, L01305, doi:10.1029/2009GL041576.
- Kanitpanyacharoen, W., D. Y. Parkinson, F. De Carlo, F. Marone, M. Stampanoni, R. Mokso, A. MacDowell, and H. R. Wenk (2013), A comparative study of X-ray tomographic microscopy on shales at different synchrotron facilities: ALS, APS and SLS, *J. Synchrotron Radiat.*, *20*(1), 172–180.

- Karagadde, S., P. D. Lee, B. Cai, J. L. Fife, M. A. Azeem, K. M. Kareh, and R. C. Atwood (2015), Transgranular liquation cracking of grains in the semi-solid state, *Nat. Commun.*, *6*, 8300.
- Kareh, K. M., P. D. Lee, R. C. Atwood, T. Connolley, and C. M. Gourlay (2014), Revealing the micromechanisms behind semi-solid metal deformation with time-resolved X-ray tomography, *Nat. Commun.*, *5*, 4464.
- Kobchenko, M., H. Panahi, F. F. Renard, D. K. Dysthe, A. Malthes-Sørenssen, A. Mazzini, and P. Meakin (2011), 4D imaging of fracturing in organic-rich shales during heating, *J. Geophys. Res.*, *116*, B12201, doi:10.1029/2011JB008565.
- Kyrieleis, A., V. Titarenko, M. Ibison, T. Connolley, and P. J. Withers (2011), Region-of-interest tomography using filtered backprojection: Assessing the practical limits, *J. Microscopy*, *241*(1), 69–82.
- Lash, G. G., and T. Engelder (2005), An analysis of horizontal microcracking during catagenesis: Example from the Catskill Delta complex, *AAPG Bull.*, *89*(11), 1433–1449.
- Lee, P. D., and J. D. Hunt (1997), Hydrogen porosity in directional solidified aluminium-copper alloys: In situ observation, *Acta Mater.*, *45*(10), 4155–4169.
- Michels, R., P. Landais, R. P. Philp, and B. E. Torkelson (1994), Effects of pressure on organic matter maturation during confined pyrolysis of Woodford kerogen, *Energy Fuel*, *8*(3), 741–754.
- Morgans-Bell, H. S., A. L. Coe, S. P. Hesselbo, H. C. Jenkyns, G. P. Weedon, J. E. Marshall, R. V. Tyson, and C. J. Williams (2001), Integrated stratigraphy of the Kimmeridge Clay Formation (Upper Jurassic) based on exposures and boreholes in south Dorset, UK, *Geol. Mag.*, *138*(05), 511–539.
- Olson, J. E. (2004), Predicting fracture swarms—The influence of subcritical crack growth and the crack-tip process zone on joint spacing in rock, *Geol. Soc. Lond. Spec. Publ.*, *231*(1), 73–88.
- Oschmann, W. (1988), Kimmeridge Clay sedimentation—A new cyclic model, *Palaeogeogr. Palaeoclimatol. Palaeoecol.*, *65*, 217–251.
- Ozkaya, I. (1988), A simple analysis of oil-induced fracturing in sedimentary rocks, *Mar. Pet. Geol.*, *5*, 293–297.
- Panahi, H., P. Meakin, F. Renard, M. Kobchenko, J. Scheibert, A. Mazzini, B. Jamtveit, A. Malthes-Sørenssen, and D. K. Dysthe (2012), A 4D Synchrotron X-Ray-Tomography Study of the Formation of Hydrocarbon- Migration Pathways in Heated Organic-Rich Shale, *SPE J.*, *18*, 366–377, doi:10.2118/162939-PA.
- Patrusheva, N., Pervukhina, M., Lebedev, M., Dautriat, J., and Dewhurst, D. N. (2014), Changes in microstructure and elastic properties of Mancos Shale after pyrolysis, 76th EAGE Conference and Exhibition 2014.
- Pervukhina, M., Y. Uvarova, A. Yurikov, N. Patrusheva, J. Dautriat, D. N. Dewhurst, and M. Lebedev (2015), Changes in microstructure and mineralogy of organic-rich shales caused by heating, *ASEG Ext. Abstr.*, *2015*(1), 1–4.
- Poissant, J., and F. Barthelat (2009), A novel “subset splitting” procedure for digital image correlation on discontinuous displacement fields, *Exp. Mech.*, *50*(3), 353–364.
- Puncreobutr, C., P. D. Lee, R. W. Hamilton, and A. B. Phillion (2012), Quantitative 3D characterization of solidification structure and defect evolution in Al alloys, *JOM*, *64*(1), 89–95.
- Puncreobutr, C., P. D. Lee, R. W. Hamilton, B. Cai, and T. Connolley (2013), Synchrotron tomographic characterization of damage evolution during aluminum alloy solidification, *Metall. Mater. Trans. A*, *44*(12), 5389–5395.
- Ramanampisoa, L., and J. R. Disnar (1994), Primary control of paleoproduction on organic matter preservation and accumulation in the Kimmeridge rocks of Yorkshire (UK), *Org. Geochem.*, *21*, 1153–1167.
- Réthoré, J., N. Limodin, J.-Y. Buffiere, F. Hild, W. Ludwig, and S. Roux (2011), Digital volume correlation analyses of synchrotron tomographic images, *J. Strain Anal. Eng. Des.*, *46*(7), 683–695.
- Schneider, P., and D. H. Eberly (2002), *Geometric Tools for Computer Graphics*, Morgan Kaufmann, Amsterdam, Netherlands.
- Teixeira, M. G., F. Donze, F. Renard, H. Panahi, E. Papachristos, and L. Scholtes (2017), Microfracturing during primary migration in shales, *Tectonophysics*, *694*, 268–279.
- Titarenko, V., R. Bradley, C. Martin, P. J. Withers, and S. Titarenko (2010), Regularization methods for inverse problems in X-ray tomography, S. R. Stock (Ed.), *SPIE Optical Engineering+ Applications—International Society for Optics and Photonics*, 78040Z.
- Tyson, R. V. (1989), Late Jurassic palynofacies trends, Piper and Kimmeridge Clay Formations, UK onshore and northern North Sea, in *Northwest European Micropalaeontology and Palynology*, edited by D. J. Batten and M. C. Keen, pp. 135–72, Halsted Press, New York.
- Tyson, R. V. (2004), Variation in marine total organic carbon through the type Kimmeridge Clay Formation (Late Jurassic), Dorset, UK, *J. Geol. Soc. London*, *161*, 667–673.
- Uvarova, Y., A. Yurikov, M. Pervukhina, M. Lebedev, V. Shulakova, M. B. Clennell, and D. N. Dewhurst (2014), Microstructural characterisation of organic-rich shale before and after pyrolysis, *APPEA J.*, *54*, 249–258.
- van Dongen, B. E., S. Schouten, and J. S. S. Damsté (2006), Preservation of carbohydrates through sulfurization in a Jurassic euxinic shelf sea: Examination of the Blackstone Band TOC cycle in the Kimmeridge Clay Formation, UK, *Org. Geochem.*, *37*(9), 1052–1073.
- van Kaam-Peters, H. M. E., S. Schouten, J. Koster, and J. S. S. Damsté (1998), Controls on the molecular and carbon isotopic composition of organic matter deposited in a Kimmeridgian euxinic shelf sea: Evidence for preservation of carbohydrates through sulfurisation, *Geochim. Cosmochim. Acta*, *62*, 3259–3283.
- Wackertapp, J., S. Hergarten, and H. J. Neugebauer (2000), A model for propagation and concentration of microcracks, *Geophys. Res. Lett.*, *27*(12), 1771–1774, doi:10.1029/1999GL010476.
- Wallisch, P., M. E. Lusignan, M. D. Benayoun, T. I. Baker, A. S. Dickey, and N. G. Hatsopoulos (2014), *MATLAB for Neuroscientists: An Introduction to Scientific Computing in MATLAB*, Academic Press, Cambridge, Mass.
- Yurikov, A., M. Pervukhina, V. Shulakova, Y. Uvarova, M. Lebedev, and B. Gurevich (2013), Fracturing of organic-rich shale during heating, in *Proceedings of the 11th SEGJ International Symposium*, pp. 390–393, Soc. of Explor. Geophys. of Japan, Yokohama, Japan, 18–21 Nov.
- Zargari, S., T. M. Wilkinson, C. E. Packard, and M. Prasad (2016), Effect of thermal maturity on elastic properties of kerogen, *Geophysics*, *81*(2), M1–M6.